



Cite as

Nano-Micro Lett.

(2025) 17:125

Received: 24 October 2024  
Accepted: 24 December 2024  
© The Author(s) 2025

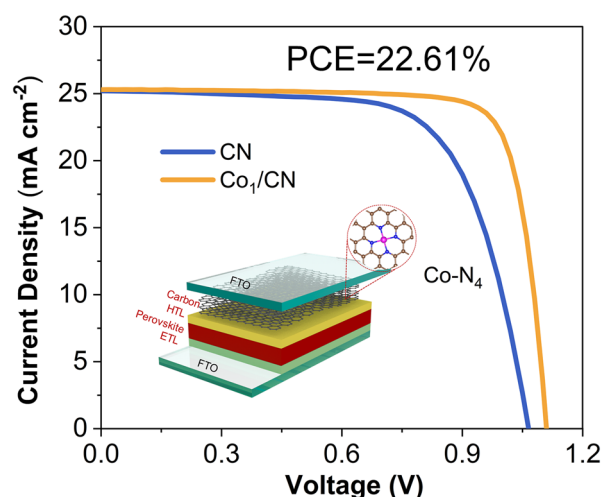
# Atomically Dispersed Metal Atoms: Minimizing Interfacial Charge Transport Barrier for Efficient Carbon-Based Perovskite Solar Cells

Yanying Shi<sup>1</sup>, Xusheng Cheng<sup>2</sup>, Yudi Wang<sup>1</sup> ✉, Wenrui Li<sup>1</sup>, Wenzhe Shang<sup>1</sup>, Wei Liu<sup>1</sup>, Wei Lu<sup>1</sup>, Jiashuo Cheng<sup>1</sup>, Lida Liu<sup>1</sup>, Yantao Shi<sup>1</sup> ✉

## HIGHLIGHTS

- Atomically dispersed metal atoms effectively enhance energy level alignment and reduce energy losses at the electrode interfaces.
- The optimized carbon-based perovskite solar cells achieve a power conversion efficiency (PCE) of 22.61% and maintain 94.4% of their initial PCE after 1000 h under continuous illumination without encapsulation.

**ABSTRACT** Carbon-based perovskite solar cells (C-PSCs) exhibit notable stability and durability. However, the power conversion efficiency (PCE) is significantly hindered by energy level mismatches, which result in interfacial charge transport barriers at the electrode-related interfaces. Herein, we report a back electrode that utilizes atomically dispersed metallic cobalt (Co) in carbon nanosheets (Co<sub>1</sub>/CN) to adjust the interfacial energy levels. The electrons in the d-orbitals of Co atoms disrupt the electronic symmetry of the carbon nanosheets (CN), inducing a redistribution of the electronic density of states that leads to a downward shift in the Fermi level and a significantly reduced interfacial energy barrier. As a result, the C-PSCs using Co<sub>1</sub>/CN as back electrodes achieve a notable PCE of 22.61% with exceptional long-term stability, maintaining 94.4% of their initial efficiency after 1000 h of continuous illumination without encapsulation. This work provides a promising universal method to regulate the energy level of carbon electrodes for C-PSCs and paves the way for more efficient, stable, and scalable solar technologies toward commercialization.



**KEYWORDS** Perovskite solar cells; Carbon electrode; Charge transport; Energy level alignment

✉ Yudi Wang, wangyd@dlut.edu.cn; Yantao Shi, shiyantao@dlut.edu.cn

<sup>1</sup> State Key Laboratory of Fine Chemicals, Frontier Science Center for Smart Materials, School of Chemistry, Dalian University of Technology, Dalian 116024, People's Republic of China

<sup>2</sup> School of Narcotics Control and Public Order Studies, Criminal Investigation Police, University of China, Shenyang 110854, People's Republic of China



## 1 Introduction

Despite the rapid advancements in perovskite solar cells (PSCs) efficiency, achieving high stability and durability in these devices remains a significant challenge [1–5]. In carbon-based perovskite solar cells (C-PSCs), carbon electrodes, characterized by stable C–C covalent bonds, effectively suppress undesirable reactions that undermine device stability [6–10]. For example, they mitigate the corrosion between metal electrodes and halide ions [11–14], as well as other harmful chemical reactions triggered by halide ion migration, thus preventing the degradation of the perovskite solar cells [15–18]. However, C-PSCs face substantial challenges in attaining high power conversion efficiency (PCE) comparable to their metal-based counterparts [19–22]. The main barrier arises from energy losses at the electrode interfaces, which can be attributed to three key factors: First, carbon electrodes exhibit inherently lower conductivity compared to metals, resulting in slower charge transport; second, they present a higher density of both macroscopic and microscopic defects, which notably trap and scatter charges; and third, there is an energy level mismatch between the carbon electrodes and adjacent functional layers.

Traditional doping methods that employ non-metal atoms, such as phosphorus (P), oxygen (O), and boron (B), can partially modulate the work function and conductivity of carbon materials [23–28], thus improving the performance of the device. For example, doping multi-walled carbon nanotubes with boron (B) to better align the energy levels at the perovskite/carbon interface has been shown to increase the efficiency of C-PSCs from 10.7% to 15.2% [26]. Additionally, an oxygen management strategy that increases the oxygen content in carbon black enhances energy level alignment at the perovskite/carbon interface, substantially improving hole extraction. This approach increased the open-circuit voltage ( $V_{oc}$ ) from 0.88 to 0.98 V, thereby boosting the PCE from 13.6% to 15.7% [27]. Building on these advancements, carbon-based single-atom materials (CSAMs) present even greater electrical tunability due to several factors: a wider selection of metals, more diverse and controllable coordination structures, and the rich structural diversity of the carbon substrates. Although most CSAMs have been applied in catalysis, only a few research teams have investigated their potential in solid-state optoelectronic devices [29, 30], where promising results have been observed. Nevertheless,

the potential of CSAMs in the optoelectronic field remains largely unexplored and demands further development.

Hence, we present the use of CSAMs as the back electrode in C-PSCs. Specifically, atomically dispersed metallic Co is anchored to nitrogen (N) atoms on carbon nanosheets ( $Co_1/CN$ ) in a well-defined  $Co-N_4$  configuration. Density functional theory (DFT) calculations reveal that the electrons in the d-orbitals of Co atoms disrupt the electronic symmetry of the carbon nanosheets (CN), inducing a redistribution of the electronic density of states that leads to a downward shift in Fermi level and a significantly reduced interfacial energy barrier, which aligns with our experimental findings. Consequently,  $Co_1/CN$ -based devices achieved an impressive PCE of 22.61% in C-PSCs. It provides a promising universal method to improve the PCE of C-PSCs and will also enable advances in large-scale production of such materials and devices across a wide range of applications.

## 2 Experimental Section

### 2.1 Materials

All materials and reagents were obtained from commercial suppliers without further purification. The materials used included  $HC(NH_2)_2I$  (FAI, Greatcell Energy, Australia),  $CH_3NH_3Cl$  (MACI, Xi'an Yuri Solar Co., Ltd., China), lead iodide ( $PbI_2$ , Advanced Electron Technology Co., Ltd., China), and 2,2',7,7'-tetrakis (N,N-dimethoxyphenylamine)-9,9'-spirobifluorene (Spiro-OMeTAD, Borun New Material Technology Co., Ltd., China). Additionally, 4-tert-butylpyridine (TBP, TCI, Japan) was also used. Moreover, bis(trifluoromethane)sulfonimide lithium salt (Li-TFSI), anhydrous dimethylformamide (DMF), anhydrous dimethyl sulfoxide (DMSO), anhydrous chlorobenzene (CB), and anhydrous isopropyl alcohol (IPA) were all purchased from Sigma-Aldrich, USA. Fluorine-doped tin dioxide (FTO,  $15 \Omega \text{ sq}^{-1}$ ) was custom-made by Suzhou Shangyang Solar Technology Co., Ltd., China. Glucose (from Shanghai Aladdin Biochemical Technology Co., Ltd.), melamine (from Tianjin Damao Chemical Reagent Factory), acetylacetonate cobalt (from Shanghai Aladdin Biochemical Technology Co., Ltd.), and potassium chloride (from Tianjin Damao Chemical Reagent Factory) were also used.

## 2.2 Preparation of $\text{Co}_1/\text{CN}$ and CN

The  $\text{Co}_1/\text{CN}$  material was synthesized using a molten salt-assisted pyrolysis method. Initially, 1.0 g of glucose and 1.0 g of melamine were used as carbon and nitrogen precursors, respectively, while 10.0 g of potassium chloride (KCl) was used as the molten salt medium. A precise amount of cobalt acetylacetonate was prepared for incorporation into the system. All solid components were combined and transferred into a ball milling jar with an appropriate amount of milling beads. The mixture was ball-milled at a frequency of 50 Hz for 5 min, repeating the process for five cycles to ensure thorough homogenization of the solid mixture. After ball milling, the homogeneous powder was separated from the milling beads and transferred to an alumina boat. The sample was placed in a tube furnace and calcined under an argon atmosphere. Calcination was conducted at 900 °C for 6 h with a controlled heating rate of 3 °C  $\text{min}^{-1}$ . Once the furnace cooled to room temperature, the resulting solid underwent acid washing with 1 M hydrochloric acid (HCl) to remove residual salts and unwanted metal particles. The washed solid was filtered, dried, and collected as a black powder designated as  $\text{Co}_1/\text{CN}$ . This method enables kilogram-scale production. For comparison, the CN sample was synthesized using the same procedure, but without the addition of cobalt acetylacetonate. This process yielded CN, the cobalt-free counterpart for subsequent analyses.

## 2.3 Fabrication of Modular $\text{Co}_1/\text{CN}$ and CN C-PSCs

Fluorine-doped tin oxide (FTO) substrates ( $1.9 \times 1.9 \text{ cm}^2$ ) were initially sonicated in deionized water, ethanol, and isopropanol for at least 10 min. After cleaning, the substrate was dried at 60 °C in an oven and treated with UV-ozone for 15 min to enhance surface wettability and remove organic impurities. Next, 40  $\mu\text{L}$  of  $\text{SnO}_2$  sol was deposited onto the conductive substrate and spin-coated at 2000 rpm for 30 s. The substrate was briefly annealed at 80 °C for 10 min. Then, 100  $\mu\text{L}$  of ammonia solution ( $\text{NH}_3 \cdot \text{H}_2\text{O}$ ) was gently added, left to stand for 10 s, and spin-coated at 2000 rpm for 20 s to remove excess ammonia. The substrate was annealed again at 80 °C for 100 min. All processes were conducted under ambient conditions ( $\text{RH} \approx 30\%$ ). The perovskite layer was prepared via a two-step method. In a nitrogen-filled glove box, 1.5 M  $\text{PbI}_2$  was dissolved in a DMF/DMSO

mixed solvent (9:1 volume ratio) and stirred at 100 °C for 30 min. Separately, 270 mg of FAI and 36 mg of MAI were dissolved in 3 mL of isopropanol (IPA) and stirred for 30 min. Both precursor solutions were filtered through 0.22  $\mu\text{m}$  PTFE filters before use. The prepared  $\text{SnO}_2$  electron transport layer (ETL) was treated with UV-ozone for 15 min. In the nitrogen glove box, 35  $\mu\text{L}$  of  $\text{PbI}_2$  precursor solution was spin-coated at 1500 rpm for 30 s and annealed at 70 °C for 40 s to form the  $\text{PbI}_2$  layer. After cooling, 100  $\mu\text{L}$  of the organic salt precursor solution was spin-coated at 1700 rpm for 30 s and annealed at 90 °C for 20 s. The films were then annealed at 150 °C for 15 min under ambient conditions ( $\text{RH} \approx 30\%$ ). For preparing the hole transport layer (HTL) solution, 43.38 mg of Spiro-OMeTAD was dissolved in 600  $\mu\text{L}$  of chlorobenzene. Once fully dissolved, 17.5  $\mu\text{L}$  of TBP and 10.5  $\mu\text{L}$  of a lithium salt-acetonitrile solution (520  $\text{mg mL}^{-1}$ ) were added sequentially. Then, 12  $\mu\text{L}$  of Spiro-OMeTAD solution was spin-coated onto the perovskite layer to form the HTL. A carbon slurry, either based on CN or  $\text{Co}_1/\text{CN}$ , was sprayed onto the assembled half-cell (FTO/ETL/perovskite/HTL) and the FTO substrate, followed by heating on a hot plate at 85 °C to facilitate solvent evaporation. The resulting half-cell A (FTO/ETL/perovskite/HTL/carbon) and collector B (FTO/carbon) were stacked together using retaining clips to form a modular C-PSC.

## 2.4 Characterizations

X-ray diffraction (XRD) was conducted using a SmartLab 9KW diffractometer with Cu  $\text{K}\alpha$  X-rays ( $\lambda = 1.5406 \text{ \AA}$ ) to obtain phase information. Field emission transmission electron microscopy (TEM) images were acquired using an F200 from Japan Electronics Co., Ltd. (JEOL). Inductively coupled plasma optical emission spectroscopy (ICP-OES) was performed on an Optima 2000DV from PerkinElmer. X-ray photoelectron spectroscopy (XPS) experiments were carried out using an ESCALB XI+ from Thermo Fisher Scientific. High-angle annular dark-field scanning transmission electron microscopy (HAADF-STEM) and corresponding energy-dispersive spectroscopy (EDS) mapping analyses were performed on a JEOL ARM-200F(S) TEM, which is equipped with a CEOS CESCOR aberration corrector and operates at an accelerating voltage of 80 kV. The convergence semi-angle and acquisition semi-angle for ADF imaging were 28–33 and 68–280 mrad, respectively. The

microstructures of the carbon electrodes were observed using a field-emission scanning electron microscope (JSM-7610F Plus, Hitachi, Japan). XPS measurements were conducted using a  $K\alpha$  X-ray photoelectron spectrometer (Thermo Scientific). Photoluminescence (PL) measurements were carried out using an FLS1000 spectrometer (Edinburgh Instruments, UK). The thickness of the carbon films was measured using atomic force microscopy (AFM) with a Dimension FastScan system (Bruker, USA).

## 2.5 X-Ray Absorption Fine Structure Measurements

The X-ray absorption fine structure (XAFS) spectra at the Co K-edge were collected at the BL14W1 beamline of the Shanghai Synchrotron Radiation Facility (SSRF). Data acquisition was performed in fluorescence mode utilizing a Lytle detector, while corresponding reference samples were collected in transmission mode. The samples were ground and uniformly applied to a specialized adhesive tape. Hard X-rays were monochromatized using a Si(111) double-crystal monochromator, and harmonic rejection mirrors were employed for detuning to eliminate harmonics. All samples were pelletized into disks with a diameter of 8 mm, and the XAFS spectra were recorded in fluorescence mode with the Lytle detector. The acquired EXAFS data were processed following standard procedures using the ATHENA module within the IFEFFIT software package. The  $k^2$ -weighted  $\chi(k)$  data in  $k$ -space, ranging from 2.5 to 10.6  $\text{\AA}^{-1}$ , were Fourier transformed into real ( $R$ ) space using a Hanning window ( $dk = 1.0 \text{\AA}^{-1}$ ) to distinguish the EXAFS contributions from different coordination shells. Effective backscattering amplitudes  $F(k)$  and phase shifts  $\Phi(k)$  for all fitting paths were calculated using the ab initio code FEFF8.0.

## 2.6 Characterization of Solar Cells

Electrochemical impedance spectroscopy (EIS) measurements were conducted under dark conditions utilizing an electrochemical workstation (Zennium Zahner, Germany). The current density–voltage ( $J$ – $V$ ) curves, which reflect the photovoltaic performance of carbon-based perovskite solar cells (C-PSCs), were obtained using a Source

Measure Unit (SMU) instrument (2400, Keithley Series, USA) under AM 1.5G 1-sun illumination ( $100 \text{ mW cm}^{-2}$ ) provided by a solar simulator (Sol3A Class AAA, Oriol, Newport, USA) in an ambient atmosphere. Before testing, the intensity of the solar light source was calibrated against an ISO-17025 standard calibrated reference silicon cell (91150 V-KG3, Newport, USA), and the active area of the device during measurements was defined using a metal mask with an area of  $0.049 \text{ cm}^2$ . The external quantum efficiency (EQE) spectra were recorded with a quantum efficiency measurement system (QE-R, Enlitech, China). To assess the long-term operational stability of the carbon-based perovskite solar cells, a photovoltaic attenuation test system (PVL-6001 M-16A, Suzhou D&R Instruments Co., Ltd., China) was employed, which operated under maximum power point (MPP) tracking and a continuous white LED light source (1-sun intensity) within a nitrogen glove box.

## 3 Result and Discussion

### 3.1 Synthesis and Characterization of $\text{Co}_1/\text{CN}$ CSAMs via Molten Salt-Mediated Pyrolysis

In this work, we successfully synthesized  $\text{Co}_1/\text{CN}$  CSAMs using a molten salt-mediated pyrolysis method. The detailed synthesis process is depicted in Fig. 1a. Specifically, melamine ( $\text{C}_3\text{H}_6\text{N}_6$ ) and glucose ( $\text{C}_6\text{H}_{12}\text{O}_6$ ) were used as nitrogen and carbon sources, respectively. Cobalt acetylacetonate ( $\text{C}_{10}\text{H}_{16}\text{CoO}_4$ ) served as the metal precursor, while potassium chloride (KCl) acted as an auxiliary medium during pyrolysis. The precursor materials were subjected to pyrolysis under an argon atmosphere in a tubular furnace. After thermal treatment, the resulting solid mixture was ground, acid-washed, filtered, and dried to yield the target sample,  $\text{Co}_1/\text{CN}$ . A control sample (CN) was prepared using the same procedure but without the addition of the metal precursor (see Experimental Section for details).

To confirm successful synthesis and assess the structural integrity of the  $\text{Co}_1/\text{CN}$  and CN samples, we first conducted XRD analysis, shown in Fig. 1b. Both samples exhibited characteristic diffraction peaks corresponding to graphitic carbon, with no detectable peaks from other phases [31]. The absence of additional peaks suggests

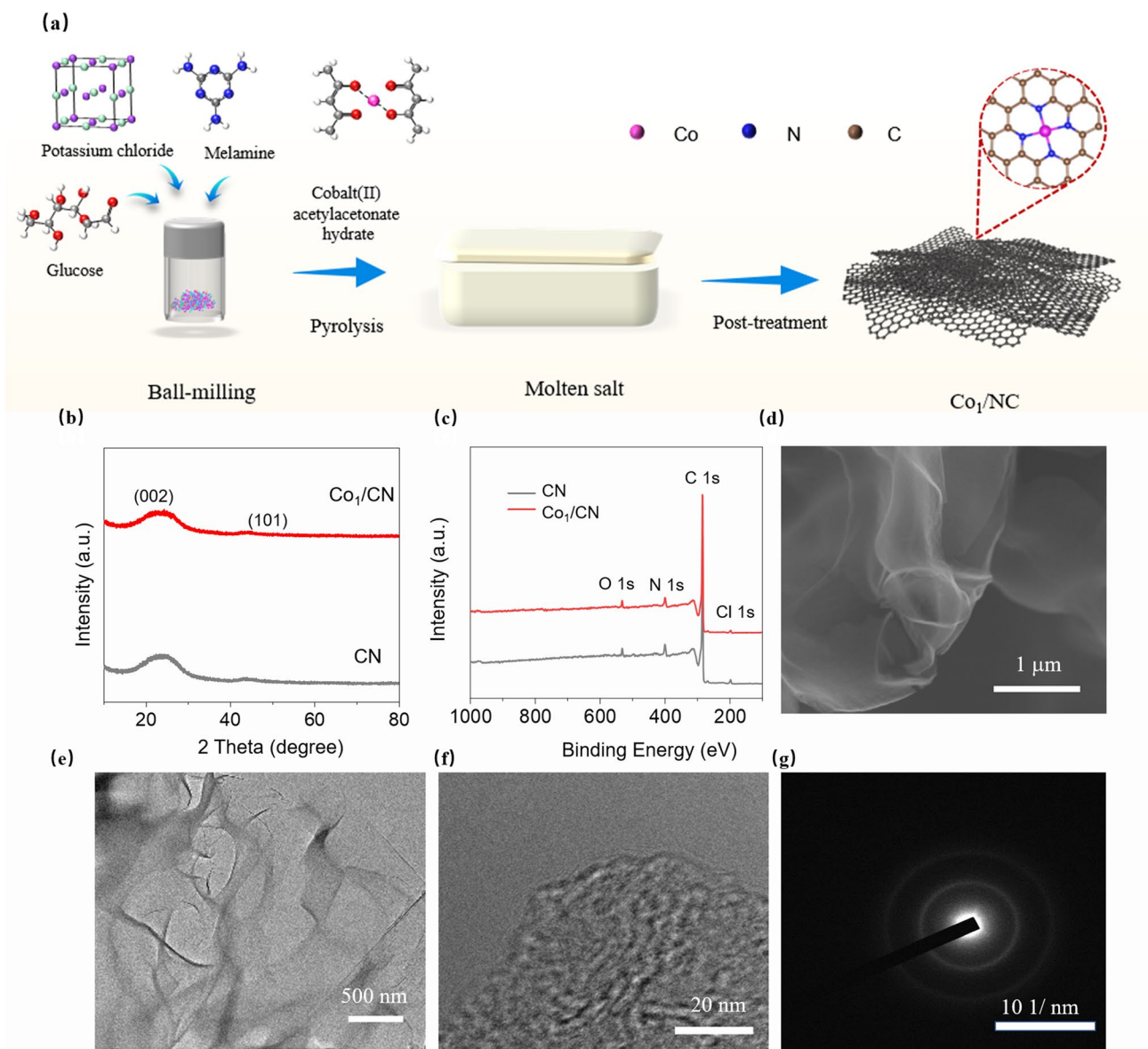


**Fig. 1** Synthesis and Characterization of  $\text{Co}_1/\text{CN}$  CSAMs. **a** Schematic illustration of the synthesis process for  $\text{Co}_1/\text{CN}$  via molten salt-mediated pyrolysis. **b** XRD patterns of CN and  $\text{Co}_1/\text{CN}$  samples. **c** XPS spectra of CN and  $\text{Co}_1/\text{CN}$  samples. **d** SEM image showing the morphology of the  $\text{Co}_1/\text{CN}$  sample. **e**, **f** HRTEM image showing the morphology of the  $\text{Co}_1/\text{CN}$  sample. **g** Selected area electron diffraction (SAED) pattern of the  $\text{Co}_1/\text{CN}$  sample

that Co atoms in the  $\text{Co}_1/\text{CN}$  material are likely present in very low concentrations and are highly anchored on the CN. Given the low Co content inferred from XRD results, we conducted an ICP-OES analysis to precisely quantify the Co concentration in  $\text{Co}_1/\text{CN}$  (Fig. S1). The analysis revealed a Co content of 0.8 wt%, confirming the low concentration of Co and supporting the hypothesis of atomic anchored on the CN. To further investigate the elemental

composition and confirm the state of Co in the samples, we conducted XPS analysis (Fig. 1c). The detailed elemental composition, determined by XPS, is presented in Table S1.

The morphology of the synthesized materials was examined by SEM (Fig. 1d). Both NC and  $\text{Co}_1/\text{CN}$  samples exhibited a wrinkled, sheet-like morphology, with no significant pores observed on the surface; moreover, the morphology did not change substantially after Co loading.

This suggests that the presence of Co does not significantly alter the overall morphology of the carbon support. The AFM image in Fig. S2 reveals that the few-layer Co<sub>1</sub>/CN sheet-like morphology has a randomly measured thickness of approximately 1.21 nm. TEM analysis (Fig. 1e, f) provided further evidence of the ultrathin CN, showing no large defects or pores, consistent with SEM observations. High-resolution TEM (Fig. 1f) revealed the stacking of multilayer graphene sheets, while the corresponding selected area electron diffraction (SAED) pattern (Fig. 1g) showed no crystalline diffraction spots, indicating that the material is predominantly amorphous. These results imply that Co atoms are atomically dispersed within the carbon matrix.

### 3.2 Fine Structure Analysis of Co<sub>1</sub>/CN CSAMs

The atomic dispersion of Co atoms on Co<sub>1</sub>/CN was confirmed by HAADF-STEM (Fig. 2a). The resulting images displayed bright spots uniformly distributed throughout the CN, which correspond to Co atoms. To further investigate the chemical states of elements, XPS analysis was conducted in the Co<sub>1</sub>/CN sample (Fig. 2b). The Co 2*p* spectrum of Co<sub>1</sub>/CN in Fig. S3 indicates the successful incorporation of Co atoms. Additionally, the deconvoluted N 1*s* spectrum revealed five distinct peaks corresponding to oxidized nitrogen (402.8 eV), graphitic nitrogen (401.2 eV), pyrrolic nitrogen (399.8 eV), pyridinic nitrogen (398.4 eV), and Co–N bonds (399.1 eV) [32–34].

X-ray absorption spectroscopy was employed to study the coordination of Co in Co<sub>1</sub>/CN. Figure 2c displays the X-ray absorption near-edge structure (XANES) spectra of the Co K-edge in Co foil, CoPc, CoO, and Co<sub>1</sub>/CN. The XANES spectra reveal distinct absorption peaks at positions A1 to A4, characteristic of Co atoms coordinated with pyridinic nitrogen. This observation suggests that the Co atoms in the Co<sub>1</sub>/CN sample are predominantly coordinated by nitrogen atoms in a planar configuration, similar to the coordination observed in cobalt phthalocyanine (CoPc). Furthermore, the energy position of the absorption edge in Co<sub>1</sub>/CN closely aligns with that of CoPc, indicating that the oxidation state of Co in the sample is primarily +2. The Fourier-transformed extended X-ray absorption fine structure (FT-EXAFS) spectra, presented in Fig. 2d, provide additional confirmation of the local atomic structure. The pronounced

peak at approximately 1.36 Å corresponds to the first coordination shell of Co–N bonds, signifying that the Co atoms are directly coordinated with nitrogen atoms in the carbon matrix. This coordination is characteristic of CSAMs, where metal atoms are stabilized by strong metal–nitrogen interactions, preventing aggregation into nanoparticles. The absence of a peak at around 2.17 Å, which would correspond to Co–Co bonds, further confirms that the Co atoms are atomically dispersed and not clustered, reinforcing the conclusion that Co<sub>1</sub>/CN functions as a CSAMs. Quantitative curve-fitting analysis was performed using different two-shell structural models: (a) Co–N and Co–C shell, (b) Co–N and Co–Co shell. Based on our comprehensive fittings, we found that the curve-fitting results using the structural models with and without the contribution of Co–C show a big difference. As shown in Figs. 2e, f and S4, also in Table S2, the structure model including the Co–C scatter gives the minor FT peak at about 1.90 Å (without phase shift correction). The fitted interatomic distance  $R_{\text{Co-C}}$  at 2.54 Å matches well with the second-shell Co–C in atomic Co<sub>1</sub>-N<sub>4</sub>C<sub>4</sub> moiety [35]. In contrast, the two-shell Co–N and Co–Co structural model gives rise to rather negative (-36.6 eV) inner potential shift ( $\Delta E_0$ ) of the Co–Co scatter, indicating that the fit is unrealistic. Therefore, the contribution from the Co–N and Co–C scatters could be evident, and we can safely conclude that a dominant majority of Co atoms are in the form of isolated Co<sub>1</sub>-N<sub>4</sub> species in the Co<sub>1</sub>/CN sample.

### 3.3 Electronic Properties of Co<sub>1</sub>/CN Electrode

The electronic structures of CN and Co<sub>1</sub>/CN were investigated using DFT calculations. As shown by the partial density of states (PDOS) analyses in Fig. 3a, b, the significantly higher electron density of Co<sub>1</sub>/CN near the Fermi level compared to CN indicates higher electrical conductivity. Additionally, the electronic density of states in the Co<sub>1</sub>/CN system exhibits pronounced spin polarization. The electrons in the d-orbitals of Co atoms disrupt the electronic symmetry of the CN, inducing a redistribution of the electronic density of states that leads to a shift in the Fermi level. Furthermore, the band structure analysis supports these findings (Figs. S5 and S6). The band structure of undoped CN shows a distinct bandgap, reinforcing its non-metallic character. However, the introduction of Co atoms transforms the band structure, with the bandgap near the Fermi level either

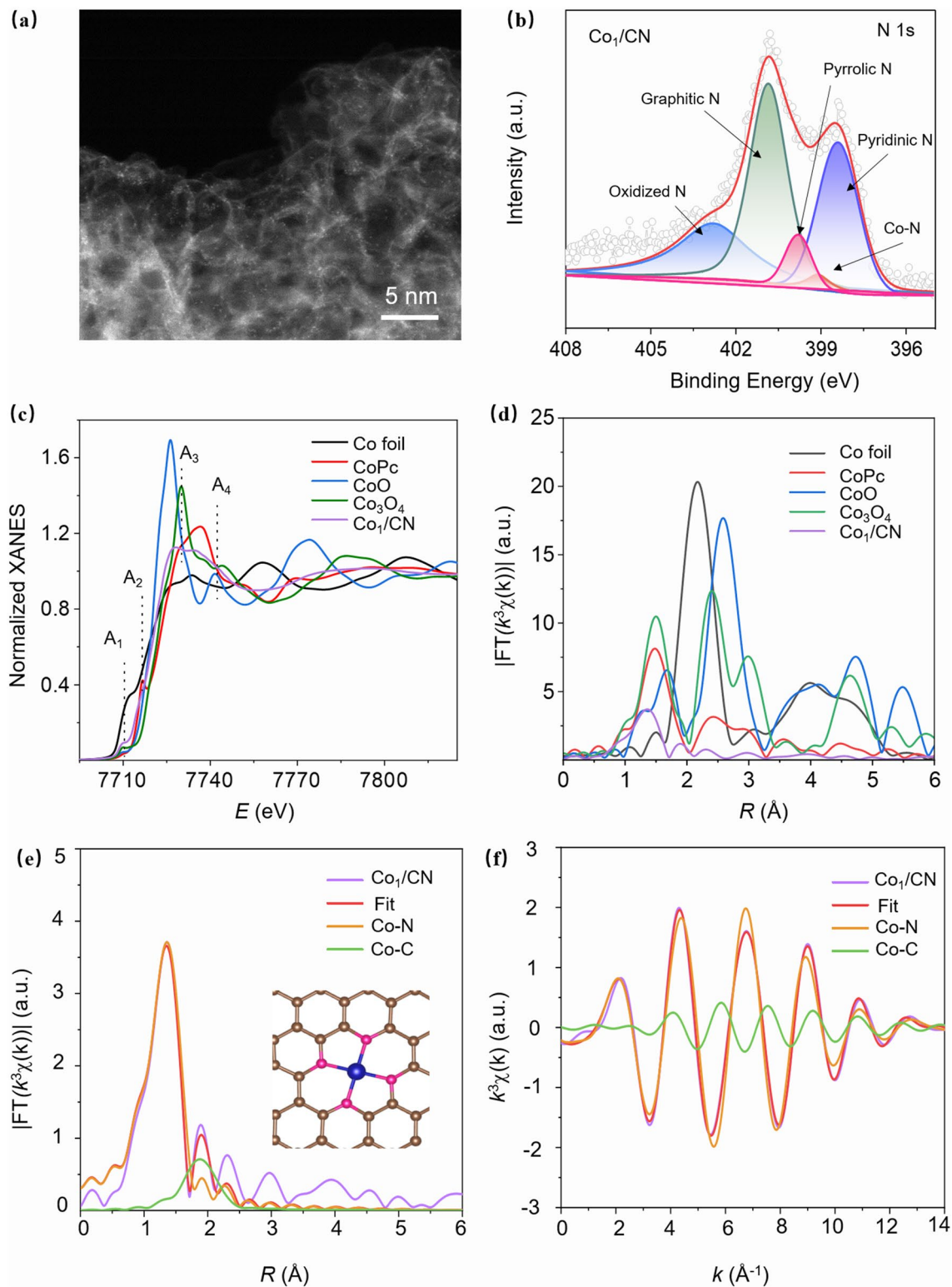


**Fig. 2** Fine Structure Analysis of  $\text{Co}_1/\text{CN}$  CSAMs **a** HAADF-STEM image of the  $\text{Co}_1/\text{CN}$  sample. **b** XPS N 1s spectrum of the  $\text{Co}_1/\text{CN}$  sample, showing the deconvoluted peaks corresponding to various nitrogen species. **c** Normalized X-ray absorption near-edge structure (XANES) spectra at the Co K-edge for  $\text{Co}_1/\text{CN}$  and reference samples. **d** Fourier-transformed extended X-ray absorption fine structure (FT-EXAFS) spectra at the Co K-edge for  $\text{Co}_1/\text{CN}$  and reference samples. **e** FT-EXAFS fitting curve of the  $\text{Co}_1/\text{CN}$  sample, with the inset showing the proposed coordination structure. **f**  $k^3$ -weighted EXAFS oscillation ( $\chi(k)$ ) and fitting curve for the  $\text{Co}_1/\text{CN}$  sample

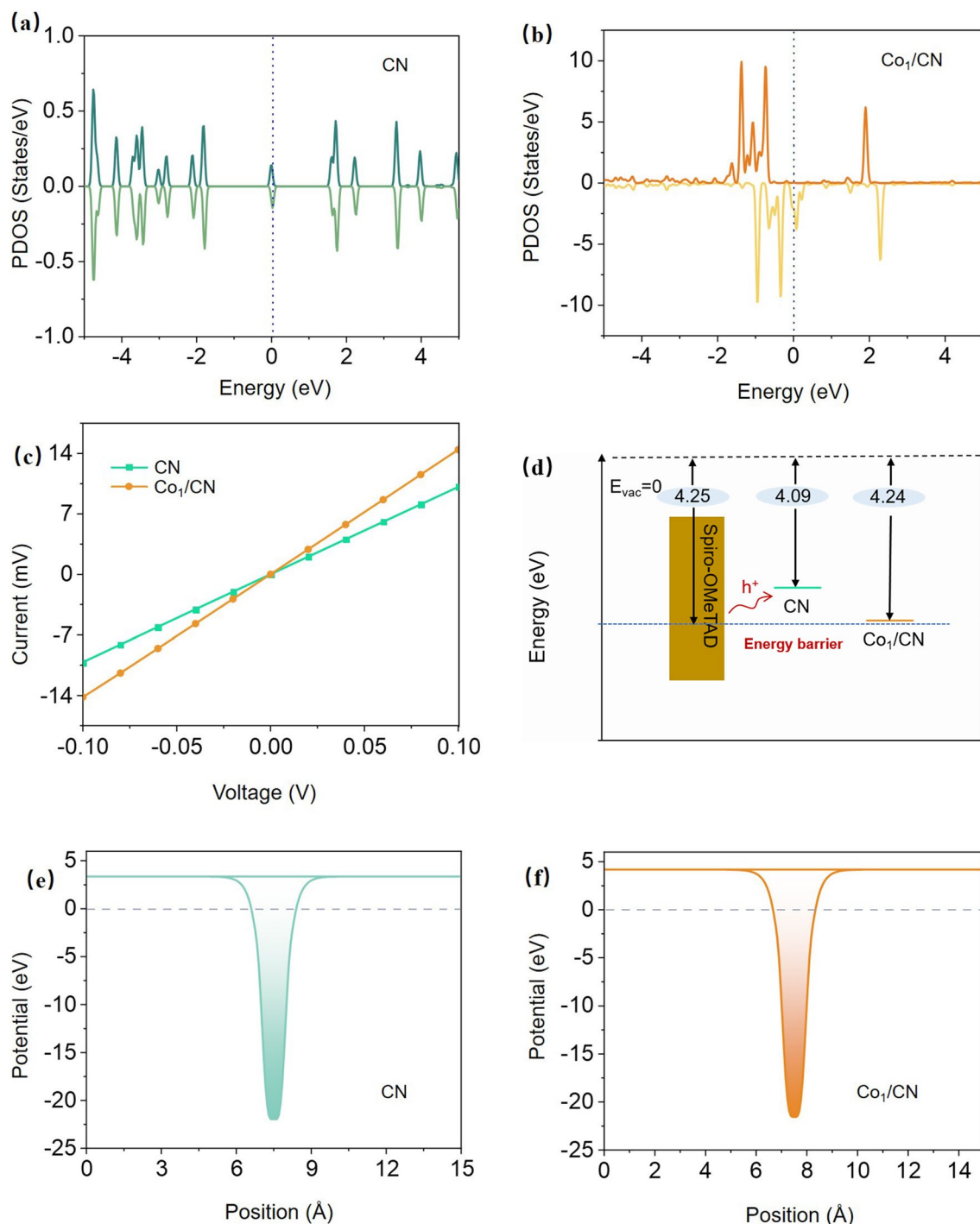


**Fig. 3** Electronic Properties of Co<sub>1</sub>/CN and CN samples. The partial density of states (PDOS) for **a** CN and **b** Co<sub>1</sub>/CN. **c** LSV characteristics of CN and Co<sub>1</sub>/CN. **d** Schematic representation of the energy levels. **e, f** Electrostatic potential profile for CN and Co<sub>1</sub>/CN along the z-direction

closing or substantially reducing, indicating a transition to metallic behavior. The electrostatic potential along the z-axis and detailed parameters were calculated for CN and Co<sub>1</sub>/CN. The theoretical calculations of the work function

(Fig. 3e, f) show an increase from 3.37 eV for CN to 4.17 eV for Co<sub>1</sub>/CN. Ultraviolet photoelectron spectroscopy (UPS) analysis demonstrated an increase in the work function from 4.09 eV for CN to 4.24 eV for Co<sub>1</sub>/CN (Fig. S7). The



energy difference between the Fermi levels of CN and Spiro-OMeTAD (Fermi level:  $-4.25$  eV) [36] was  $0.16$  eV, potentially creating a significant energy barrier for charge transfer. However,  $\text{Co}_1/\text{CN}$  reduced this difference to just  $0.01$  eV, effectively minimizing the energy barrier and facilitating more efficient hole transfer at the interface (Fig. 3d). These theoretical predictions are corroborated by linear sweep voltammetry (LSV) measurements, where devices with an FTO/ $\text{Co}_1/\text{CN}$  structure exhibit significantly steeper slopes compared to those with FTO/CN (Figs. 3c and S8). This indicates that the  $\text{Co}_1/\text{CN}$  sample shows a notably higher current density and, therefore, superior conductivity relative to undoped CN, especially at lower voltages, consistent with the DFT-calculated band structure analysis. Additionally, four-point probe resistance measurements further confirm this enhanced conductivity, as  $\text{Co}_1/\text{CN}$  exhibits significantly lower sheet resistance compared to the CN sample. Specifically, the conductivity of  $\text{Co}_1/\text{CN}$  (approximately  $15,000$  S  $\text{cm}^{-1}$ ) is more than twice that of CN (approximately  $7,000$  S  $\text{cm}^{-1}$ ) (Fig. S9).

### 3.4 Performance Evaluation of $\text{Co}_1/\text{CN}$ as an Electrode Material in Perovskite Solar Cells

The photovoltaic performance of PSCs incorporating  $\text{Co}_1/\text{CN}$  as an electrode material was systematically evaluated using n-i-p structured devices. These devices consisted of FTO/ $\text{SnO}_2$ /Perovskite/Spiro-OMeTAD/ $\text{Co}_1/\text{CN}$  for half-cell A and FTO/ $\text{Co}_1/\text{CN}$  for half-cell B, stacked under controlled pressure (Fig. S10). A cross-sectional SEM image of the device interface, displayed in Fig. S11, shows the thickness and morphology of the perovskite layer on top. The CN-based devices exhibited significant enhancements, achieving a maximum PCE of  $18.35\%$ , an open-circuit voltage ( $V_{\text{oc}}$ ) of  $1.07$  V, a short-circuit current density ( $J_{\text{sc}}$ ) of  $25.20$  mA  $\text{cm}^{-2}$ , and a fill factor ( $FF$ ) of  $68.07\%$  (Fig. S12). Specifically, the optimized Co content of  $\text{Co}_1/\text{CN}$ -based devices achieved a PCE of  $22.61\%$ , a  $V_{\text{oc}}$  of  $1.11$  V, a  $J_{\text{sc}}$  of  $25.30$  mA  $\text{cm}^{-2}$ , and an  $FF$  of  $80.51\%$  (Figs. 4a, b and S13). We have conducted a more detailed comparative analysis of the  $\text{Co}_1/\text{CN}$  electrodes against other common back electrode materials used in similar applications, as shown in Table S3. Furthermore, the  $\text{Co}_1/\text{CN}$ -based devices of external quantum efficiency (EQE) measurements closely matched the  $J_{\text{sc}}$  values obtained from  $J$ - $V$  testing (Figs. 4c

and S14). Additionally, steady-state power output (SPO) measurements were conducted under continuous one-sun illumination to assess the long-term operational stability of the devices. The  $\text{Co}_1/\text{CN}$ -based devices achieved a stabilized power output of  $21.78\%$  at their maximum power point ( $V_{\text{max}}$ ) after  $100$  s of illumination, significantly outperforming the control devices. This result underscores the superior stability and sustained performance of the  $\text{Co}_1/\text{CN}$ -based devices under practical operating conditions (Fig. 4d). To ensure the reproducibility of these findings, multiple devices (20 control and 20 targets) were fabricated and tested. Statistical analysis revealed consistent improvements in  $V_{\text{oc}}$ ,  $FF$ , and SPO across different batches, underscoring the reliability of the performance enhancements (Figs. 4e and S15).

The improvement in  $V_{\text{oc}}$  is primarily attributed to the enhanced energy level alignment between the  $\text{Co}_1/\text{CN}$  electrode and the Spiro-OMeTAD layer, as evidenced by UPS analysis. This improved alignment effectively reduces the interfacial energy barrier, thereby facilitating more efficient charge transfer and consequently increasing  $V_{\text{oc}}$ . Photoluminescence and time-resolved PL measurements were conducted using a glass/perovskite/Spiro-OMeTAD/carbon test structure (Fig. S16). The faster charge transfer observed with  $\text{Co}_1/\text{CN}$  electrodes can be attributed to the atomic-level dispersion of Co, enabling precise tuning of energy levels at the electrode/perovskite interface and improved energy level alignment. This reduces energy barriers and minimizes recombination at the interface, ensuring efficient charge transfer. Moreover, Mott-Schottky analysis (Fig. 4f) reveals that the built-in potential ( $V_{\text{bi}}$ ) of the control and  $\text{Co}_1/\text{CN}$ -based devices is  $0.95$  and  $0.98$  V, respectively, indicating an enhanced driving force for carrier transfer in the treated devices. Concurrently, the enhanced conductivity of the  $\text{Co}_1/\text{CN}$  CSAM, as demonstrated by both DFT calculations and LSV measurements, shows a significant increase in the density of states near the Fermi level and a steeper slope in the LSV curves, which leads to a reduction in series resistance and directly contributes to the improved  $FF$ . To analyze the impact on charge transfer dynamics, EIS was conducted on the C-PSCs, measured under dark conditions using the configuration shown in Fig. 4g at a bias of  $0$  V. Two distinct arcs are observed in the Nyquist plots, with their spans qualitatively reflecting the resistance associated with charge transfer and charge recombination kinetics. Compared to CN-based devices,  $\text{Co}_1/\text{CN}$ -based

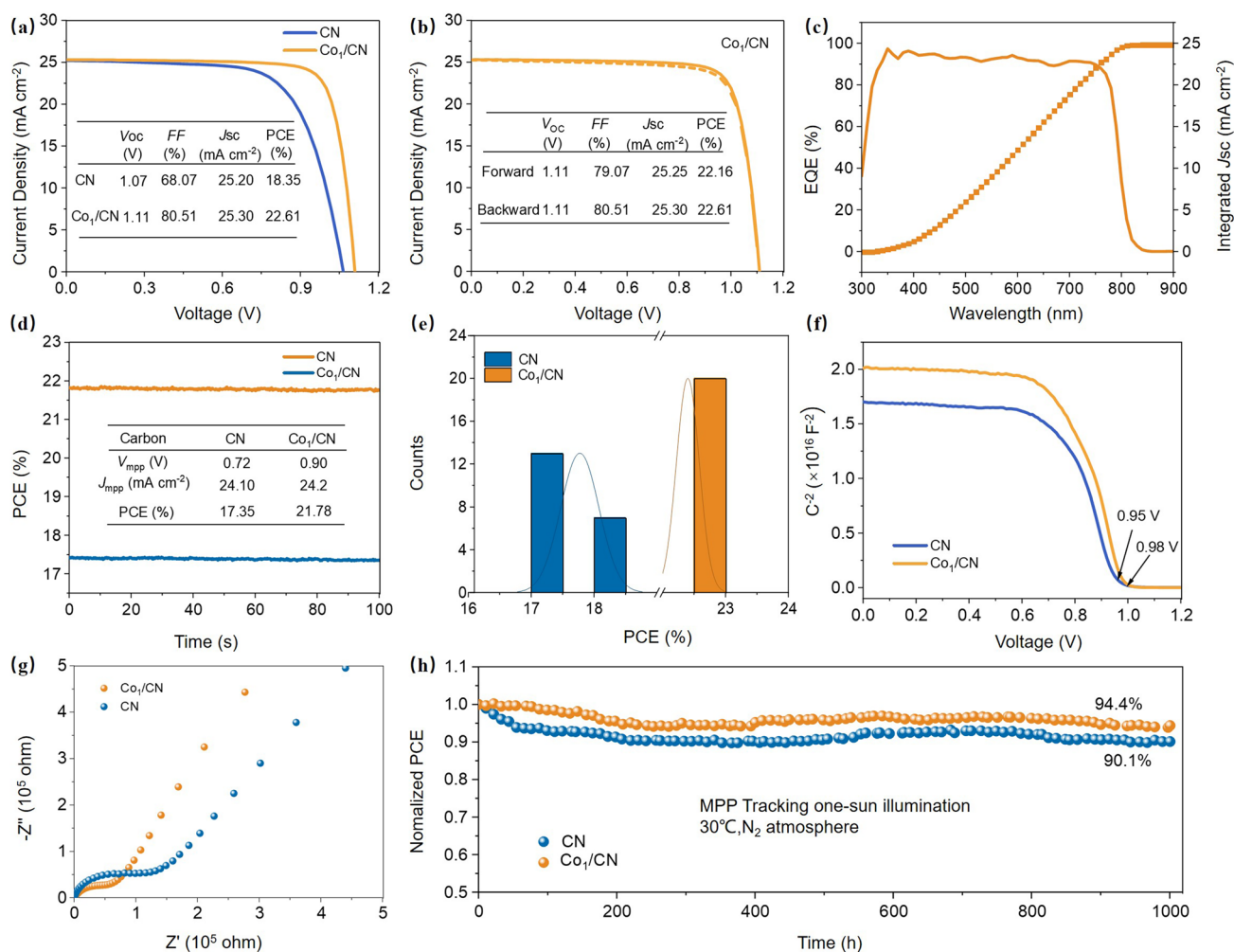


**Fig. 4** Performance evaluation of  $\text{Co}_1/\text{CN}$  as an electrode material in perovskite solar cells. **a** Current density–voltage ( $J$ - $V$ ) curves of the CN and  $\text{Co}_1/\text{CN}$ -based devices under standard one-sun illumination ( $\text{AM } 1.5\text{G}$ ,  $100 \text{ mW cm}^{-2}$ ). **b** Forward and backward  $J$ - $V$  curves of the CN and  $\text{Co}_1/\text{CN}$ -based devices. **c** EQE spectra and the corresponding integrated  $J_{sc}$  for CN and  $\text{Co}_1/\text{CN}$ -based devices, demonstrating the spectral response across different wavelengths. **d** Stability test showing the PCE over time for CN and  $\text{Co}_1/\text{CN}$ -based devices. **e** Statistical distribution of PCE for CN and  $\text{Co}_1/\text{CN}$ -based devices. **f** Capacitance–voltage ( $C$ - $V$ ) characteristics of the CN and  $\text{Co}_1/\text{CN}$ -based devices, indicating the built-in potential ( $V_{bi}$ ) derived from the Mott–Schottky analysis. **g** Nyquist plots derived from EIS measurements for CN and  $\text{Co}_1/\text{CN}$ -based devices. **h** Operational stability of the encapsulated C-PSC devices under continuous one-sun illumination

devices exhibit smaller charge transfer resistance ( $R_{tr}$ ) and larger charge recombination resistance ( $R_{rec}$ ), both critical for high PCE. For quantitative assessment, Nyquist plots were fitted using a standard equivalent circuit to extract detailed impedance parameters (see Fig. S17). The  $\text{Co}_1/\text{CN}$ -based devices demonstrate significantly lower sheet resistance  $R_s$  (from 24.50 to 22.85  $\Omega \text{ cm}^2$ ), confirming enhanced conductivity of  $\text{Co}_1/\text{CN}$ . The reduced  $R_{tr}$  (from 110.3 to 54.76  $\text{k}\Omega \text{ cm}^2$ ) is attributed to interfacial charge transfer enabled by better energy level alignment, contributing to the observed increase in  $V_{oc}$ . Additionally, the

increased  $R_{rec}$  (from 5126 to 6137  $\text{k}\Omega \text{ cm}^2$ ) indicates that interfacial charge recombination in the  $\text{Co}_1/\text{CN}$  devices has been effectively suppressed, further supporting superior performance. Furthermore, dark  $J$ - $V$  measurements indicate that  $\text{Co}_1/\text{CN}$ -based devices exhibit lower dark current densities, implying better rectification and reduced leakage currents (Fig. S18). This is further corroborated by transient photovoltage (TPV) measurements under open-circuit conditions (Fig. S19), which show a prolonged carrier lifetime from 0.19 to 0.39 ms, suggesting suppressed charge carrier recombination. These improvements in

leakage current suppression and charge carrier dynamics collectively contribute to achieving a higher  $FF$ .

These findings, supported by both theoretical and experimental analyses, underscore the effectiveness of  $\text{Co}_1/\text{CN}$  as an advanced electrode material in significantly enhancing the overall performance of PSCs. We further investigated the impact of  $\text{Co}_1/\text{CN}$  on the operational stability of the device, assessing stability by tracking the maximum power point (MPP) under simulated one-sun illumination (Fig. 4h). The unencapsulated  $\text{Co}_1/\text{CN}$ -based device retained 94.4% of its initial PCE after 1000 h of continuous operation. More importantly, this study underscores the potential of CSAMs as outstanding candidates for use as electrode or interfacial layers in all-solid-state photovoltaics, likely to attract considerable interest in future research.

## 4 Conclusions

In summary, we demonstrated a significant advancement in C-PSC through the introduction of atomically dispersed metallic Co on carbon nanosheets ( $\text{Co}_1/\text{CN}$ ) as an innovative back electrode. This approach effectively addressed the challenge of energy level mismatches that typically hinder the PCE of C-PSCs. The Co atoms interact with the electronic structure of CN, redistributing the electronic density of states and shifting the Fermi level downward. This adjustment led to a substantial reduction in the interfacial energy barrier, thereby improving charge transport at the electrode interfaces. Consequently,  $\text{Co}_1/\text{CN}$ -based devices achieved an impressive PCE of 22.61% in C-PSCs, coupled with remarkable long-term stability. These findings highlight the potential of CSAMs to regulate the energy levels of carbon electrodes, offering a versatile and scalable solution for enhancing both efficiency and stability in C-PSCs.

**Acknowledgements** The work was supported by the National Natural Science Foundation of China (22109019, 52272193) and Fundamental Research Funds for the Central Universities (DUT-22LAB602, DUT23RC(3)002)

**Authors' Contributions** Y. Shi and Y. Wang conceived and supervised this project. Y. Shi prepared the solar cells, did the structural characterization, and tested the performance. X. Cheng prepared the samples. W. Li, J. Cheng, and L. Liu performed electrochemical measurements. W. Shang developed the theoretical calculation, performed the analytic calculations, and performed the numerical simulations. W. Liu analyzed the fine structure of samples. W. Lu is responsible for drawing the picture. R. Cai and Z. Sun at the

Instrumental Analysis Center of Dalian University performed the fluorescence experiments and AFM analyses. Y. Shi wrote the manuscript with contributions from all authors. All authors discussed the manuscript and proposed suggestions for revision.

## Declarations

**Conflict of Interest** The authors declare no interest conflict. They have no known competing financial interests or personal relationships that could have appeared to influence the work reported in this paper.

**Open Access** This article is licensed under a Creative Commons Attribution 4.0 International License, which permits use, sharing, adaptation, distribution and reproduction in any medium or format, as long as you give appropriate credit to the original author(s) and the source, provide a link to the Creative Commons licence, and indicate if changes were made. The images or other third party material in this article are included in the article's Creative Commons licence, unless indicated otherwise in a credit line to the material. If material is not included in the article's Creative Commons licence and your intended use is not permitted by statutory regulation or exceeds the permitted use, you will need to obtain permission directly from the copyright holder. To view a copy of this licence, visit <http://creativecommons.org/licenses/by/4.0/>.

**Supplementary Information** The online version contains supplementary material available at <https://doi.org/10.1007/s40820-024-01639-3>.

## References

1. T. Liu, M.M.S. Almutairi, J. Ma, A. Stewart, Z. Xing et al., Solution-processed thin film transparent photovoltaics: Present challenges and future development. *Nano-Micro Lett.* **17**, 49 (2025). <https://doi.org/10.1007/s40820-024-01547-6>
2. Y. Wang, W. Li, Y. Yin, M. Wang, W. Cai et al., Defective MWCNT enabled dual interface coupling for carbon-based perovskite solar cells with efficiency exceeding 22%. *Adv. Funct. Mater.* **32**(31), 2204831 (2022). <https://doi.org/10.1002/adfm.202204831>
3. H. Ma, M. Wang, Y. Wang, Q. Dong, J. Liu et al., Asymmetric organic diammonium salt buried in  $\text{SnO}_2$  layer enables fast carrier transfer and interfacial defects passivation for efficient perovskite solar cells. *Chem. Eng. J.* **442**, 136291 (2022). <https://doi.org/10.1016/j.cej.2022.136291>
4. M. Ma, C. Zhang, Y. Ma, W. Li, Y. Wang et al., Efficient and stable perovskite solar cells and modules enabled by tailoring additive distribution according to the film growth dynamics (article). *Nano-Micro Lett.* **17**, 39 (2025). <https://doi.org/10.1007/s40820-024-01538-7>
5. J. Zhuang, J. Wang, F. Yan, Review on chemical stability of lead halide perovskite solar cells (review). *Nano-Micro Lett.* **15**, 84 (2023). <https://doi.org/10.1007/s40820-023-01046-0>
6. M. Forouzandeh, M. Heidariramsheh, H.R. Heydarnezhad, H. Nikbakht, M. Stefanelli et al., Enhanced carbon-based



- back contact electrodes for perovskite solar cells: Effect of carbon paste composition on performance and stability. *Carbon* **229**, 119450 (2024). <https://doi.org/10.1016/j.carbon.2024.119450>
7. Y. Ren, K. Zhang, Z. Lin, X. Wei, M. Xu et al., Long-chain gemini surfactant-assisted blade coating enables large-area carbon-based perovskite solar modules with record performance. *Nano-Micro Lett.* **15**, 182 (2023). <https://doi.org/10.1007/s40820-023-01155-w>
  8. C. Dong, B. Xu, D. Liu, E.G. Moloney, F. Tan et al., Carbon-based all-inorganic perovskite solar cells: Progress, challenges and strategies toward 20% efficiency. *Mater. Today* **50**, 239–258 (2021). <https://doi.org/10.1016/j.mattod.2021.05.016>
  9. D. Bogachuk, S. Zouhair, K. Wojciechowski, B. Yang, V. Babu, A. Hagfeldt, A. Hinsch et al., Low-temperature carbon-based electrodes in perovskite solar cells. *Energy Environ. Sci.* **13**(11), 3880–3916 (2020). <https://doi.org/10.1039/D0EE02175J>
  10. J. Cheng, H. Ma, Y. Shi, L. Liu, W. Shang et al., Single-atom Ti decorated carbon black and carbon nanotubes: modular dual-carbon electrode for optimizing the charge transport kinetics of perovskite solar cells. *Adv. Funct. Mater.* **34**, 2409533 (2024). <https://doi.org/10.1002/adfm.202409533>
  11. S. Zhang, Y. Wang, S. Li, Z. Wang, H. Chen et al., Concerning the stability of seawater electrolysis: a corrosion mechanism study of halide on Ni-based anode. *Nat. Commun.* **14**(1), 4822 (2023). <https://doi.org/10.1038/s41467-023-40563-9>
  12. J. Büttner, T. Berestok, S. Burger, M. Schmitt, M. Daub et al., Are halide-perovskites suitable materials for battery and solar-battery applications—fundamental reconsiderations on solubility, lithium intercalation, and photo-corrosion. *Adv. Funct. Mater.* **32**(49), 2206958 (2022). <https://doi.org/10.1002/adfm.202206958>
  13. D. Kong, C. Dong, X. Wei, C. Man, X. Lei et al., Size matching effect between anion vacancies and halide ions in passive film breakdown on copper. *Electrochim. Acta* **292**, 817–827 (2018). <https://doi.org/10.1016/j.electacta.2018.10.004>
  14. D. Li, X. Dong, P. Cheng, L. Song, Z. Wu et al., Metal halide perovskite/electrode contacts in charge-transporting-layer-free devices. *Adv. Sci.* **9**(36), 2203683 (2022). <https://doi.org/10.1002/advs.202203683>
  15. Y. Jiang, S.-C. Yang, Q. Jeangros, S. Pisoni, T. Moser et al., Mitigation of vacuum and illumination-induced degradation in perovskite solar cells by structure engineering. *Joule* **4**(5), 1087–1103 (2020). <https://doi.org/10.1016/j.joule.2020.03.017>
  16. S.P. Dunfield, L. Bliss, F. Zhang, J.M. Luther, K. Zhu et al., From defects to degradation: a mechanistic understanding of degradation in perovskite solar cell devices and modules. *Adv. Energy Mater.* **10**(26), 1904054 (2020). <https://doi.org/10.1002/aenm.201904054>
  17. K. Domanski, E.A. Alharbi, A. Hagfeldt, M. Grätzel, W. Tress, Systematic investigation of the impact of operation conditions on the degradation behaviour of perovskite solar cells. *Nat. Energy* **3**(1), 61–67 (2018). <https://doi.org/10.1038/s41560-017-0060-5>
  18. N. Ahn, K. Kwak, M.S. Jang, H. Yoon, B.Y. Lee et al., Trapped charge-driven degradation of perovskite solar cells. *Nat. Commun.* **7**(1), 13422 (2016). <https://doi.org/10.1038/ncomms13422>
  19. Q. Wang, D. Zheng, K. Wang, Q. Yang, X. Zhu et al., Versatile charge collection materials in perovskite photovoltaics. *Nano Energy* **128**, 109892 (2024). <https://doi.org/10.1016/j.nanoen.2024.109892>
  20. L. Perrin, E. Planes, T. Shioki, R. Tsuji, J.-C. Honore et al., How ammonium valeric acid iodide additive can lead to more efficient and stable carbon-based perovskite solar cells: Role of microstructure and interfaces? *Sol. RRL* **8**(17), 2400393 (2024). <https://doi.org/10.1002/solr.202400393>
  21. H. Kim, K.R. Pyun, M.-T. Lee, H.B. Lee, S.H. Ko et al., Recent advances in sustainable wearable energy devices with nanoscale materials and macroscale structures. *Adv. Funct. Mater.* **32**(16), 2110535 (2022). <https://doi.org/10.1002/adfm.202110535>
  22. L. Ma, Z. Bi, W. Zhang, Z. Zhang, Y. Xiao et al., Synthesis of a three-dimensional interconnected oxygen-, boron-, nitrogen-, and phosphorus tetratomic-doped porous carbon network as electrode material for the construction of a superior flexible supercapacitor. *ACS Appl. Mater. Interfaces* **12**(41), 46170–46180 (2020). <https://doi.org/10.1021/acsami.0c13454>
  23. L.K. Putri, B.-J. Ng, W.-J. Ong, H.W. Lee, W.S. Chang et al., Engineering nanoscale p–n junction via the synergetic dual-doping of p-type boron-doped graphene hybridized with n-type oxygen-doped carbon nitride for enhanced photocatalytic hydrogen evolution. *J. Mater. Chem. A* **6**(7), 3181–3194 (2018). <https://doi.org/10.1039/C7TA09723A>
  24. H. Hu, Z. Shi, K. Khan, R. Cao, W. Liang et al., Recent advances in doping engineering of black phosphorus. *J. Mater. Chem. A* **8**(11), 5421–5441 (2020). <https://doi.org/10.1039/D0TA00416B>
  25. J.P. Paraknowitsch, A. Thomas, Doping carbons beyond nitrogen: an overview of advanced heteroatom doped carbons with boron, sulphur and phosphorus for energy applications. *Energy Environ. Sci.* **6**(10), 2839–2855 (2013). <https://doi.org/10.1039/C3EE4144B>
  26. X. Zheng, H. Chen, Q. Li, Y. Yang, Z. Wei et al., Boron doping of multiwalled carbon nanotubes significantly enhances hole extraction in carbon-based perovskite solar cells. *Nano Lett.* **17**(4), 2496–2505 (2017). <https://doi.org/10.1021/acs.nanolett.7b00200>
  27. C. Tian, A. Mei, S. Zhang, H. Tian, S. Liu et al., Oxygen management in carbon electrode for high-performance printable perovskite solar cells. *Nano Energy* **53**, 160–167 (2018). <https://doi.org/10.1016/j.nanoen.2018.08.050>
  28. T. Yin, L. Long, X. Tang, M. Qiu, W. Liang et al., Advancing applications of black phosphorus and BP-analog materials in photo/electrocatalysis through structure engineering and surface modulation. *Adv. Sci.* **7**(19), 2001431 (2020). <https://doi.org/10.1002/advs.202001431>
  29. C. Zhang, S. Liang, W. Liu, F.T. Eickemeyer, X. Cai et al., Ti<sub>1</sub>-graphene single-atom material for improved energy level

- alignment in perovskite solar cells. *Nat. Energy* **6**(12), 1154–1163 (2021). <https://doi.org/10.1038/s41560-021-00944-0>
30. M. Guo, C. Wei, C. Liu, K. Zhang, H. Su et al., Composite electrode based on single-atom Ni doped graphene for planar carbon-based perovskite solar cells. *Mater. Des.* **209**, 109972 (2021). <https://doi.org/10.1016/j.matdes.2021.109972>
31. Z. Wei, Y. Liu, J. Ding, Q. He, Q. Zhang et al., Promoting electrocatalytic CO<sub>2</sub> reduction to CO via sulfur-doped Co-N-C single-atom catalyst. *Chin. J. Chem.* **41**(24), 3553–3559 (2023). <https://doi.org/10.1002/cjoc.202300372>
32. Y. Tang, J. Chen, Z. Mao, C. Roth, D. Wang, Highly N-doped carbon with low graphitic-N content as anode material for enhanced initial Coulombic efficiency of lithium-ion batteries. *Carbon Energy* **5**(2), e257 (2023). <https://doi.org/10.1002/cey2.257>
33. M. Liu, X. Zhu, Y. Song, G. Huang, J. Wei et al., Bifunctional edge-rich nitrogen doped porous carbon for activating oxygen and sulfur. *Adv. Funct. Mater.* **33**(11), 2213395 (2023). <https://doi.org/10.1002/adfm.202213395>
34. P. Yu, L. Wang, F. Sun, Y. Xie, X. Liu et al., Co Nanoislands rooted on Co-N-C nanosheets as efficient oxygen electrocatalyst for Zn-air batteries. *Adv. Mater.* **31**(30), 1901666 (2019). <https://doi.org/10.1002/adma.201901666>
35. H. Fei, J. Dong, Y. Feng, C.S. Allen, C. Wan et al., General synthesis and definitive structural identification of MN<sub>4</sub>C<sub>4</sub> single-atom catalysts with tunable electrocatalytic activities. *Nat. Catal.* **1**(1), 63–72 (2018). <https://doi.org/10.1038/s41929-017-0008-y>
36. Q. Zheng, F. Cao, Y. Wang, A. Tong, S. Wang et al., Synergistic effect of ionic liquid-doped spiro-OMeTAD: simultaneous management of energy level alignment and interfacial traps in perovskite solar cells. *Inorg. Chem. Front.* **11**(19), 6627–6637 (2024). <https://doi.org/10.1039/D4QI01459F>

**Publisher's Note** Springer Nature remains neutral with regard to jurisdictional claims in published maps and institutional affiliations.

